PAPER

Check for updates

Efficient and easily repeatable organic solar cells in a high boiling point solvent by introducing a highly mixed tolerant guest acceptor†

Xiangyu Shen,‡[ab] Xiaoning Wang,‡[bcd] Jianxiao Wang,*[bcd] Rulin Wang,*[a] Yonghai Li, [iD][bcd] Fuzhen Bi [iD]*[bcd] and Xichang Bao [iD][bcd]

Organic solar cells (OSCs) with low-temperature solution processing have attracted extensive research interest. To achieve good phase separation and molecular nucleation crystallization, the active layer usually needs to be processed with low boiling point solvents, which narrows the processing window and limits the implementation of industrial printing processes. Herein, we synthesized a novel non-fullerene acceptor **L8BO-2O** as a third component to regulate the performance of the classical **PM6:Y6** system in high boiling point solvents. **L8BO-2O**, with an alkoxy chain, can effectively suppress the aggregation effect of active materials, which is beneficial for achieving appropriate phase separation in high-boiling solvent film-forming processes. Additionally, the similar structure and stacking distance between **L8BO-2O** and **Y6** can effectively improve the mixing tolerance of the host and guest, achieve more effective energy transfer and alloy working mechanisms, thereby greatly increasing light utilization and charge extraction. Finally, the efficiency of the champion ternary OSC reached 16.4% with the doping of 20 wt% **L8BO-2O**, and the efficiencies of all the ternary OSCs were significantly improved over a wide range of doping (0–80 wt%). This result emphasizes the feasibility of introducing a suitable third component to achieve efficient and reproducible OSCs in high boiling point solvents.

Introduction

Organic solar cells (OSCs) have attracted great attention due to their advantages of light weight, flexibility and semi-transparency.[1–6] With the development of non-fullerene acceptors (NFAs), the power conversion efficiency (PCE) of single junction OSCs has been raised to over 20%.[7–12] Beyond the innovation of donor and acceptor materials, the device fabrication methods also play a critical role in improving device performance. They determine not only the phase separation scale and crystallinity on the macroscopic scale but also the intermolecular stacking pattern and stacking distance on the microscopic scale.

Only a reasonable combination of active layer materials and fabrication methods can enhance the device performance. Solvent selection is a crucial step during device fabrication.[13,14] At present, high-performance devices are treated with low boiling point chloroform solvents, but in the process of large-area device preparation, the solvent is prone to cause a sharp change in the concentration of active layer materials due to its rapid evaporation rate. An effective solution is to use high-boiling solvents, but the widely used NFAs tend to show excessive aggregation in high-boiling solvents, which seriously limits the improvement of device performance.[14,15]

The main reason for the excessive aggregation of NFAs in high-boiling solvents is their slow evaporation rate. Several strategies have been proposed to solve this issue and thus optimize the active layer morphology, such as side alkyl chain engineering,[16–20] solvent/solid additives,[21–23] hot-casting strategy[24] and introducing a third component.[25–27] Recently, the ethylene glycol ethyl methyl ether chain was attached to NFAs and the obtained compounds were used as the third component to construct ternary OSCs. The results show that this kind of compound can increase the miscibility and crystallinity of the host system and thus optimize the active layer film-formation kinetics. Finally, the excessive aggregation was effectively suppressed and the obtained device showed enhanced

a Centre for Theoretical and Computational Physics, College of Physics, Qingdao University, Qingdao 266071, China. E-mail: rulin11@qdu.edu.cn

b Key Laboratory of Photoelectric Conversion and Utilization of Solar Energy, Qingdao Institute of Bioenergy and Bioprocess Technology, Chinese Academy of Sciences, Qingdao 266101, China. E-mail: wangjianxiao@qibebt.ac.cn, bifz@qibebt.ac.cn

c Functional Laboratory of Solar Energy, Shandong Energy Institute, Qingdao 266101, China

d Qingdao New Energy Shandong Laboratory, Qingdao 266101, China

† Electronic supplementary information (ESI) available. See DOI: https://doi.org/10.1039/d4tc03192j

‡ These two authors contributed equally to this work.

This journal is © The Royal Society of Chemistry 2024

J. Mater. Chem. C, 2024, **12**, 17403–17410 | **17403**

exciton dissociation and charge transportation.[25,28,29] Ternary strategy has been widely proven to be a simple and effective way to improve device performance, and ternary OSCs still maintain the highest efficiency of single OSCs.[30–34] However, it is worth noting that the differences in the physical and chemical properties between the guest material and the host system in the ternary strategy often result in the crystallinity and morphology of the mixed phase being highly sensitive to component ratios (*i.e.*, low mixing tolerance). The proportion of the guest material to the host generally does not exceed 20 wt%. When a large proportion of the third component is doped, it will cause a sharp decline in the device performance. Therefore, in the manufacturing process of ternary OSCs, precise control of the host-to-guest ratio is required, which increases the difficulty of device fabrication to some extent. Therefore, solving the problem of excessive aggregation of active layer materials in high-boiling solvents and low mixing tolerance of the third component will be the only way to achieve large-scale industrial production.

Hence, we designed and synthesized a novel non-fullerene acceptor **L8BO-2O** based on polar oligomeric (ethylene glycol) side chains as the third component to regulate the aggregation behavior of the star system **PM6:Y6** in the high-boiling solvent chlorobenzene (CB). The characteristic polar oligomeric (ethylene glycol) side chains of **L8BO-2O** can effectively inhibit the aggregation effect of the active material, increase the miscibility of the donors and acceptors, and thus achieve appropriate phase separation in high-boiling solvent film-forming processes. The similar structure and stacking distance between **L8BO-2O** and **Y6** can effectively improve the mixing tolerance of the host and guest, achieving effective energy transfer and alloy working mechanism, thereby greatly improving the light utilization and charge extraction efficiency. As a result, under a wide doping range of **L8BO-2O** (0–80 wt% in CB solution), the performance of all ternary OSCs is significantly improved. Both

the PCE of **PM6:Y6** binary OSCs (14.54%) and PM6:**L8BO-2O:Y6** ternary OSCs (16.43%) are at the highest level of the consistent system (Table S1, ESI†). The introduction of the high mixing tolerance third component not only reduces the aggregation of the active materials in high-boiling solvents but also ensures better performance repeatability, which reduces the manufacturing difficulty of the device and lays the foundation for industrial production.

Results and discussion

The chemical structures of PM6, **Y6** and **L8BO-2O** are presented in Fig. 1a, and the synthetic routes and detailed characterizations of **L8BO-2O** are listed in the ESI.† Subsequently, the cyclic voltammetry (C–V) method was used to investigate the energy levels of the donor PM6, acceptor **Y6** and **L8BO-2O**, as shown in Fig. S14 (ESI†). A schematic diagram of energy levels is illustrated in Fig. 1b. The lowest unoccupied molecular orbital (LUMO)/highest occupied molecular orbital (HOMO) levels were found to be −3.20/−5.45, −4.10/−5.70, −3.91/−5.58 eV for PM6, **Y6** and **L8BO-2O**, respectively. The LUMO/HOMO of **L8BO-2O** lie between that of PM6 and **Y6**, which results in a cascaded energy levels alignment. The cascaded energy level alignment of the donor and acceptor can ensure efficient exciton dissociation and charge transport.[35,36] The normalized UV-vis spectra of the PM6, **Y6** and **L8BO-2O** neat films are shown in Fig. 1c. Compared with **Y6**, **L8BO-2O** exhibits a slight blue shift at the maximum, which form complementary absorption spectra and is beneficial for enhancing the photon capture ability of the ternary active layer. In addition, the absorption spectrum of the blend acceptor film (20 wt% **L8BO-2O** in **Y6**) shows a low-intensity shoulder peak at 675 nm (Fig. S15, ESI†), which indicates that the addition of **L8BO-2O** could suppress the excessive aggregation of the host acceptor. Furthermore, we measured the temperature-dependent absorption spectra for **Y6**, **L8BO-2O**, and the mixed acceptor (20 wt% **L8BO-2O** in **Y6**)
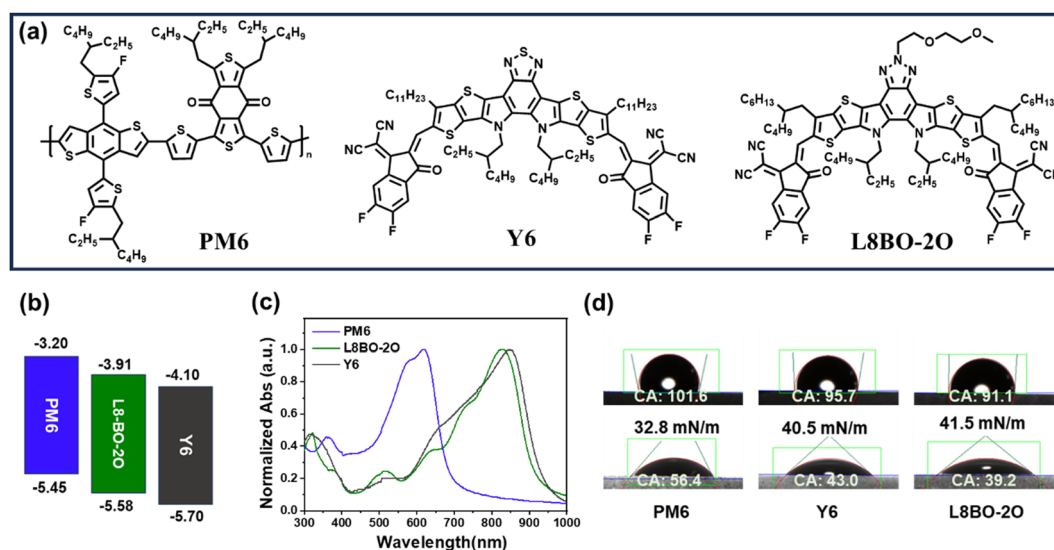

Fig. 1 (a) Chemical structures of donor PM6 and two acceptors **Y6**, **L8BO-2O**. (b) Energy levels of PM6, **Y6** and **L8BO-2O**. (c) UV–vis spectra of PM6, **Y6** and **L8BO-2O** neat films. (d) The contact angles of water (top panel) and diiodomethane (bottom panel) droplets on PM6, **Y6** and **L8BO-2O** neat films.

17404 | *J. Mater. Chem. C*, 2024, **12**, 17403–17410

This journal is © The Royal Society of Chemistry 2024

dilute solutions, respectively (Fig. S16, ESI†). With increasing temperature, all the absorption peaks exhibit a significant blue shift and the extinction coefficient decreases, indicating that the aggregation is disrupted. As shown in Fig. S18d–f (ESI†), after introducing **L8BO-2O**, the absorption of the **Y6:L8BO-2O** mixed solution showed more significant changes in the peak position and intensity compared with the corresponding films, which indicate that the intermolecular interaction between the well miscible **L8BO-2O** and the host **Y6** not only slows down the aggregation of **Y6** but also leaves space for the ordered stacking of molecules.

To further investigate the miscibility between PM6, **Y6** and **L8BO-2O**, the contact angles of water (H_2O) and diiodomethane (CH_2I_2) droplets on neat films were evaluated, as presented in Fig. 1d. The surface energy (γ_s) and Flory–Huggins interaction parameter (χ) calculated from the equation $\chi = k\left(\sqrt{\gamma_1} - \sqrt{\gamma_2}\right)^2$ are summarized in Table S2 (ESI†).[37,38] The γ_s values of PM6, **Y6** and **L8BO-2O** are 32.8, 40.5 and 41.5 mN m^{-1}, respectively. The χ_s values of PM6/**Y6** and PM6/**L8BO-2O** are 0.406 k and 0.505 k, respectively, while the χ_s between **Y6** and **L8BO-2O** is only 0.005 k. Similar surface energy and smaller χ suggest good miscibility between **Y6** and **L8BO-2O**.[39,40] To further verify the good miscibility of the two acceptors, the γ_s of the blend acceptors films with different proportions was also calculated, as shown in Fig. S17 (ESI†). It can be observed that the γ_s of the mixed acceptors is between that of the two acceptors and is approximately linear with the proportion, which indicates good miscibility between the host and guest materials, facilitating the morphology control of mixed films.

To investigate the morphology characteristic of the ternary active layer after the introduction of the **L8BO-2O** acceptor with good miscibility, atomic force microscopy (AFM) was used. The AFM images are shown in Fig. S18 (ESI†), and the corresponding root-mean-square (RMS) surface roughness values are summarized in Fig. 2a. Both trace and high proportions of third component doping can significantly reduce the roughness of the ternary blend film, which is beneficial for reducing the trap defects in the active layer and enhancing the interaction between the host and guest acceptor molecules, indicating that **L8BO-2O** can inhibit the aggregation degree of molecules during the film-formation process in high boiling point solvents.

To understand the working mechanism of **L8BO-2O** in the blend system, the time-resolved PL (TR-PL) spectra of neat and mixed acceptors films were measured, as shown in Fig. S19 (ESI†), and the fitted exciton lifetimes are summarized in Fig. 2b. Significantly, all mixed acceptors exhibit longer exciton lifetimes, which can provide sufficient time for exciton diffusion and dissociation. In addition, the steady-state PL spectra of neat and mixed acceptor films are presented in Fig. 2c. The PL peak of the **Y6** and **L8BO-2O** neat films were located at 912 and 886 nm, respectively. After adding different ratios of **L8BO-2O**, the PL intensity of the **Y6:L8BO-2O** blend films shows a slight increase, but the peak position is still the same as that of the **Y6** neat film. This phenomenon is typically explained as the energy transfer from **L8BO-2O** to **Y6**, through which the light capture achieves optimization.[41–43] The steady-state PL spectra of binary and ternary blend films were also measured, as displayed in Fig. 2d. The PL intensity of all the blend films significantly decreased compared to the neat films, which
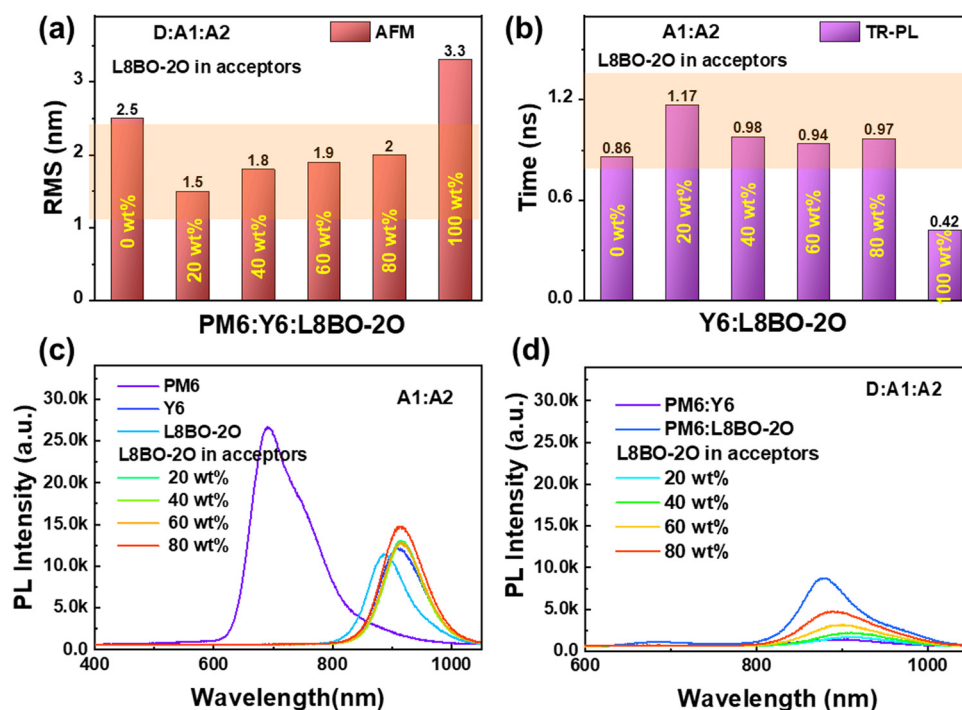

Fig. 2 (a) RMS surface roughness values of the **PM6:Y6:L8BO-2O** blend films with different **L8BO-2O** contents. (b) Exciton lifetimes of **Y6**, **L8BO-2O** and mixed acceptor films. (c) PL spectra of PM6, **Y6**, **L8BO-2O** neat films and mixed acceptor films. (d) PL spectra of binary and ternary blend films.

This journal is © The Royal Society of Chemistry 2024

J. Mater. Chem. C, 2024, 12, 17403–17410 | 17405

indicates the occurrence of effective exciton dissociation in the blend films. However, surprisingly, the PL peak position varies with the proportion of the three components in the ternary blend films, which is inconsistent with the pattern presented in the dual acceptor films. This movement of the peak position may indicate the presence of additional alloy working mechanisms between **L8BO-2O** and **Y6**, which corresponds to the formation of **L8BO-2O** and **Y6** alloy phases due to their good miscibility. To verify this point, it is necessary to further evaluate the photovoltaic performances of the device.

To investigate the impact of **L8BO-2O** on the photovoltaic performance of the devices, all binary and ternary OSCs were fabricated based on the conventional device structure of ITO/PEDOT:PSS/active layer/PDINN/Ag. The detailed parameters of the optimization process of OSCs are shown in Fig. S20 and Table S3 (ESI†). The current density–voltage (J–V) curves of the **PM6:Y6**-based OSCs with different **L8BO-2O** contents are shown in Fig. 3a, and the corresponding photovoltaic parameters are summarized in Table 1. The **PM6:Y6**-based binary OSC exhibits an advanced PCE of 14.54%, with a J_{SC} of 23.66 mA cm^{-2}, a V_{OC} of 0.82 V and an FF of 74.71%. On the other hand, for the PM6:**L8BO-2O**-based binary OSC, a PCE of 12.42%, with a J_{SC} of 19.00 mA cm^{-2}, a V_{OC} of 0.90 V and an FF of 72.3%, was delivered. Generally, the content of the third component in the ternary OSCs does not exceed 20%, which is determined by the low mixing tolerance of the selected active layer materials with different physical characteristics. A larger proportion of the third component will lead to a sharp decline in the device performance. However, whether a small or a large proportion of the third component is added, the performance of the ternary OSCs is significantly improved compared to the corresponding binary OSCs. This high mixing tolerance ensures better repeatability of the device's photovoltaic

performance (Fig. 3b). When adding 20 wt% **L8BO-2O** in the acceptors, the optimal ternary OSC achieved the highest PCE of 16.4%, with a much superior J_{SC} of 25.21 mA cm^{-2}, a V_{OC} of 0.85 V, and an FF of 76.66%. Then the external quantum efficiency (EQE) was measured to further explore the reason for the improved J_{SC}, and the EQE spectra of the binary and ternary OSCs are depicted in Fig. 3c. In comparison, all the ternary devices with **L8BO-2O** exhibited an enhanced EQE response in the visible region, which indicates that the absorption of the ternary blends are more efficiently converted to photocurrents. Slight differences between the absorption and EQE spectra are mainly due to the diffraction effect and the interference effect between the incident light and the reflected light from the Ag electrode in the active layers. The integrated J_{SC} from the EQE spectra matches well with that from the J–V curves but is slightly lower, which is the reason that the EQE is tested in ambient air without any packaging.

According to the above analysis, the **PM6:Y6:L8BO-2O**-based ternary system may have energy transfer and alloy model working mechanisms simultaneously. To further determine the working mechanism, the V_{OC} of the **PM6:Y6:L8BO-2O**-based ternary OSCs with different **L8BO-2O** contents are probed and shown in Fig. 3d. With the introduction and increase in content of the **L8BO-2O**, the V_{OC} increases approximately linearly, indicating the existence of an alloy working mechanism between **L8BO-2O** and **Y6**. Then, the J–V curves of **L8BO-2O**, **Y6** and **L8BO-2O:Y6**-based pure acceptor devices were also measured (Fig. 3e). The J_{SC} of **L8BO-2O: Y6**-based devices are between those of the **L8BO-2O/Y6**-based devices, indicating that no exciton dissociation occurs between **L8BO-2O** and **Y6**. Ultimately, **L8BO-2O** with good miscibility with **Y6** not only forms an alloy phase with **Y6** but also exhibits energy transfer from **L8BO-2O** to **Y6** in the ternary OSCs. The dual mechanism
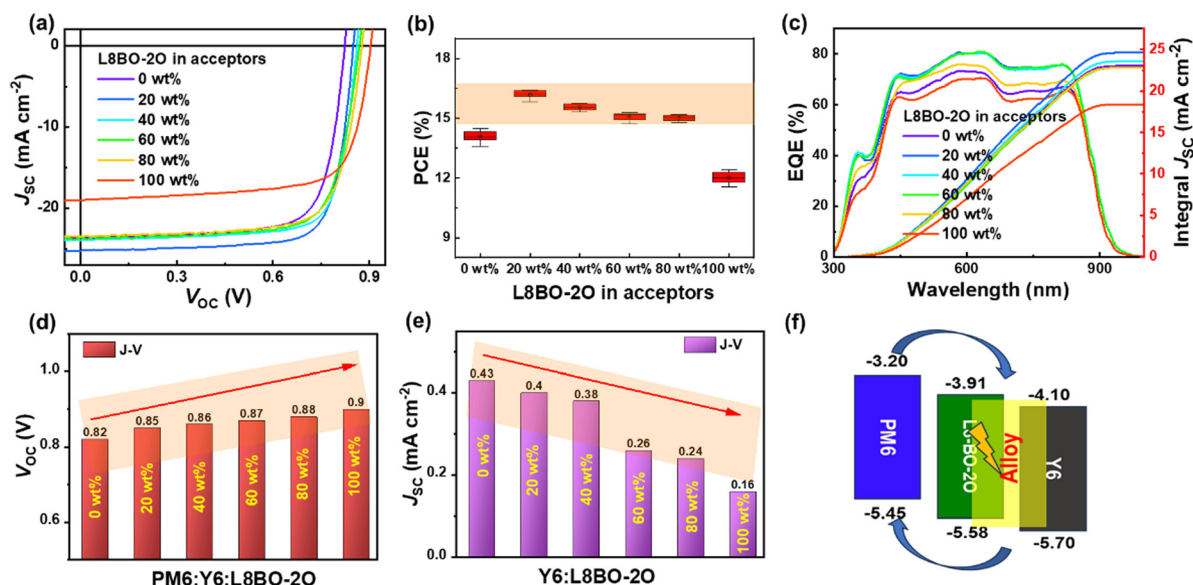

Fig. 3 (a) J–V curves, (b) device efficiency statistics obtained from ten devices, (c) the corresponding EQE spectra and (d) V_{OC}s of **PM6:Y6:L8BO-2O**-based OSCs with different **L8BO-2O** contents. (e) The J–V curves of **Y6**, **L8BO-2O** and **Y6:L8BO-2O**-based pure acceptor devices. (f) Schematic diagram of the working mechanism.

17406 | *J. Mater. Chem. C*, 2024, **12**, 17403–17410

This journal is © The Royal Society of Chemistry 2024

Table 1 Photovoltaic parameters of the **PM6:Y6:L8BO-2O**-based OSCs with different **L8BO-2O** contents

L8BO-2O in acceptors (wt%)	V_{OC} (V)	J_{SC} (mA cm^{-2})	J_{SC} (integral) (mA cm^{-2})	FF (%)	PCE^a (%)
0	0.82 (0.81 ± 0.01)	23.66 (22.3 ± 1.4)	22.99	74.71 (72.5 ± 2.2)	14.54 (14.08 ± 0.4)
20	0.85 (0.84 ± 0.01)	25.21 (23.8 ± 1.5)	24.62	76.66 (74.9 ± 1.7)	16.40 (16.21 ± 0.2)
40	0.86 (0.85 ± 0.01)	23.89 (22.5 ± 1.3)	23.57	76.54 (74.6 ± 2.0)	15.75 (15.56 ± 0.2)
60	0.87 (0.86 ± 0.01)	23.72 (22.6 ± 1.1)	22.80	74.05 (71.8 ± 2.2)	15.26 (15.07 ± 0.18)
80	0.88 (0.87 ± 0.01)	23.45 (22.2 ± 1.2)	22.78	73.89 (71.7 ± 2.1)	15.19 (15.01 ± 0.15)
100	0.90 (0.89 ± 0.01)	19.00 (17.7 ± 1.3)	18.40	72.3 (70.1 ± 2.2)	12.42 (12.01 ± 0.4)

^{a} Average and standard deviation data in parentheses are obtained from ten devices.

is illustrated in Fig. 3f. This dual mechanism optimized the exciton dissociation and charge transfer process, thereby significantly improving the photovoltaic performance of ternary OSCs under a wide proportion range of the third component.

To clarify the reasons for the high mixing tolerance of **L8BO-2O** in improving the photovoltaic performance, the photocurrent density (J_{ph}) and effective voltage (V_{eff}) curves of binary and ternary OSCs are provided in Fig. S21 (ESI†), and the parameters are listed in Table S4 (ESI†). The J_{ph} is defined as $J_{ph} = J_L − J_D$, where J_L and J_D represent the current density under illumination and dark conditions, respectively. The V_{eff} is defined as $V_{eff} = V_0 − V$, where V_0 is the voltage when $J_{ph} = 0$ mA cm^{-2} and the V is the applied voltage.[44] The saturated photocurrent density (J_{sat}) is approximately equal to J_{ph} when $V_{eff} = 1$ V. The exciton dissociation efficiency (η_{diss}) and charge collection efficiency (η_{coll}) can be approximately evaluated by J_{ph}/J_{sat}, where J_{ph} is obtained under open circuit conditions and maximum power output condition, respectively. The calculated η_{diss}/η_{coll} of PM6:Y6 and PM6:L8BO-2O binary OSC are 99.1%/87.0% and 98.3%/88.3%, respectively. After adding **L8BO-2O**, the η_{diss} and η_{coll} of the **PM6:Y6:L8BO-2O**-based ternary OSCs were considerably enhanced. The enhanced η_{diss} can be attributed to

the optimized phase separation scale of the active layer by **L8BO-2O**, and the enhanced η_{coll} is attributed to the construction of the more effective alloy-like transport channels. The synergistic enhancement of η_{diss} and η_{coll} in ternary OSC indicates more effective charge generation, charge transfer, and suppression of charge recombination, which are beneficial for improving the device J_{SC} and FF.

To further verify the improved dissociation efficiency of the device, the TR-PL spectra of binary and ternary blend films are depicted in Fig. 4a. The exciton lifetime (τ_s) of the **PM6:Y6** and PM6:L8BO-2O blend films are 0.17 and 0.25 ns, respectively. After adding **L8BO-2O**, the τ_s of the ternary blend films significantly decreased, indicating that the addition of the third component accelerated the dissociation process of excitons, which is also consistent with the above results. On the other hand, the charge recombination mechanisms of the devices are investigated by fitting the relationship between illumination intensity (P_{light}) and V_{OC}/J_{SC}. The relationship between J_{SC} and P_{light} can be expressed as $J_{SC} \propto P_{light}^s$. In addition, the relationship between V_{OC} and P_{light} can be expressed as $V_{OC} \propto nkT/q\ln(P_{light})$, where k is the Boltzmann's constant, T is absolute temperature, and q is the elementary charge. The bimolecular
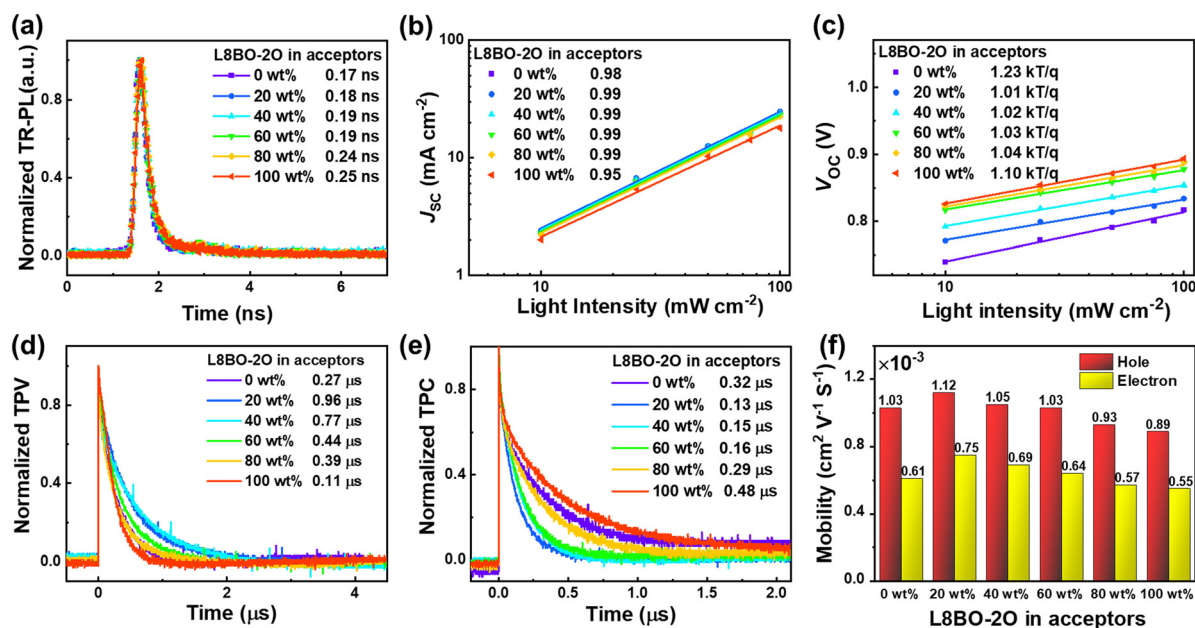

Fig. 4 (a) TR-PL curves of binary and ternary blend films. (b) J_{SC}s and (c) V_{OC}s versus light illumination intensity of the corresponding OSCs. (d) TPV and (e) TPC curves of the corresponding OSCs. (f) Hole and electron mobilities of the binary and ternary blend films.

This journal is © The Royal Society of Chemistry 2024

J. Mater. Chem. C, 2024, **12**, 17403–17410 | **17407**

recombination and trap recombination can be ignored when the s or n value approaches 1.00.[45] As shown in Fig. 4b, the s values of the **PM6:Y6**-based binary and ternary OSCs are closer to 1.00, indicating the lower bimolecular recombination. Similarly, all the n values of ternary OSCs equal nearly 1.00, indicating that the trap recombination of all ternary OSCs has been effectively suppressed compared to the **PM6:Y6**-based binary OSC (Fig. 4c).[46] Lower trap-assisted recombination and bimolecular recombination further explain the significant improvement of FF in the ternary OSCs.

The charge carrier extraction and recombination dynamics were further elucidated by transient photovoltage (TPV) and transient photocurrent (TPC). As shown in Fig. 4d, the fitted carrier lifetimes (τ_{rec}) of ternary OSCs are 0.96 μs (20 wt%), 0.77 μs (40 wt%), 0.44 μs (60 wt%) and 0.39 μs (80 wt%), which are significantly longer than that of **PM6:Y6** (0.27 μs) and PM6:**L8BO-2O** (0.11 μs)-based binary devices. Also, the fitted charge extraction times (τ_{ext}) of ternary OSCs are 0.13 μs (20 wt%), 0.15 μs (40 wt%), 0.16 μs (60 wt%) and 0.29 μs (80 wt%), which are significantly shorter than that of the

PM6:Y6 (0.32 μs) and PM6:**L8BO-2O** (0.48 μs)-based binary devices (Fig. 4e). The results signify that the introduction of **L8BO-2O** within a wide proportion range can improve charge extraction and suppress charge recombination in the active layer, thereby contributing to the achievement of more satisfactory J_{SC} and FF.

The hole and electron mobilities were measured by the space charge limited current (SCLC) method. The hole-only and electron-only devices were fabricated with the structure of ITO/PEDOT:PSS/active layer/MoO$_3$/Ag and ITO/ZnO/active layer/PDINN/Ag. The active layers were prepared under the same conditions as the OSCs. The J–V curves of hole-only and electron-only devices were measured in the dark, and the results are shown in Fig. S22 (ESI†). The calculated hole/electron mobilities of the **PM6:Y6**-based device are $1.03 \times 10^{-3}/0.61 \times 10^{-3}$ cm^2 V^{-1} s^{-1}. After adding different **L8BO-2O** contents, the hole/electron mobilities of the ternary devices were increased to $1.12 \times 10^{-3}/0.75 \times 10^{-3}$, $1.05 \times 10^{-3}/0.69 \times 10^{-3}$, $1.03 \times 10^{-3}/0.64 \times 10^{-3}$, $0.93 \times 10^{-3}/0.57 \times 10^{-3}$, and $0.89 \times 10^{-3}/0.54 \times 10^{-3}$ cm^2 V^{-1} s^{-1} for the proportion of
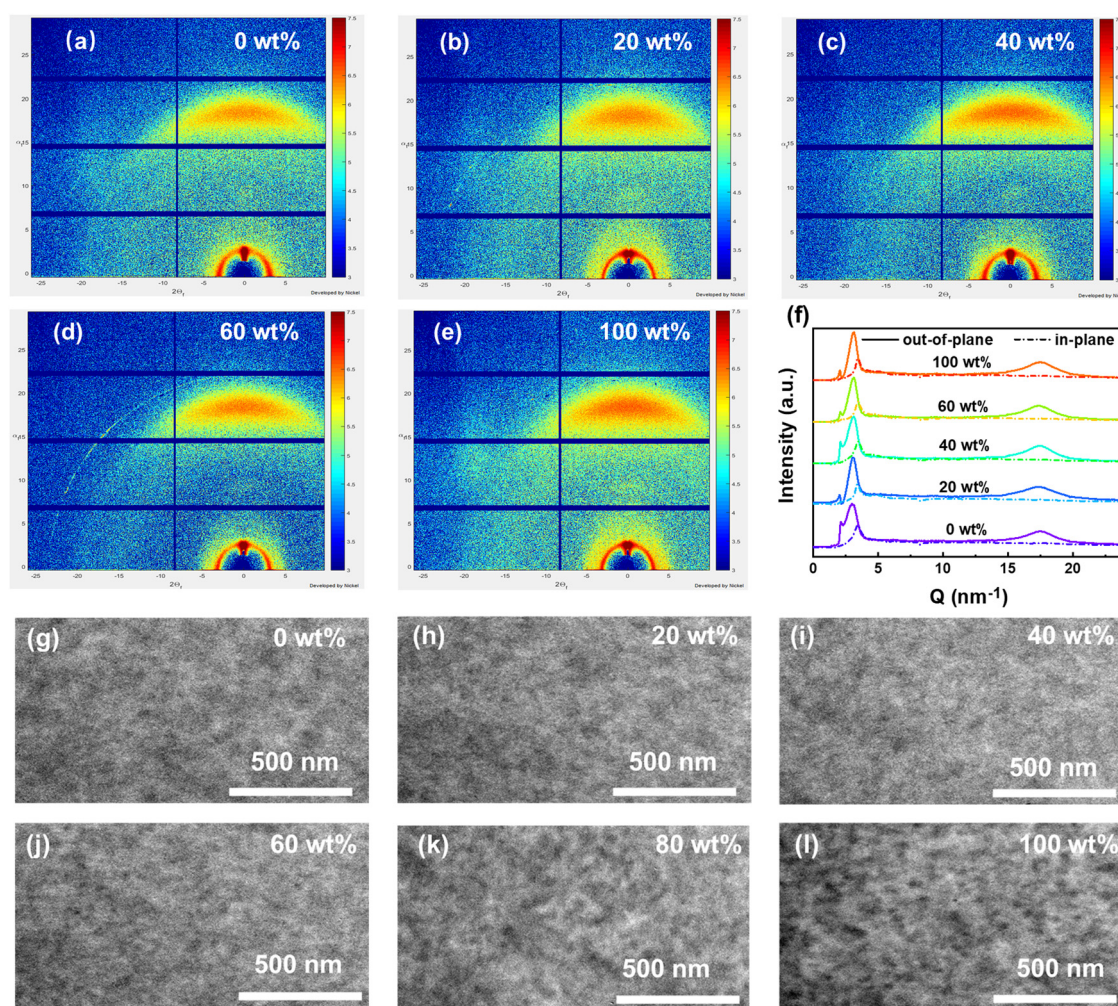

Fig. 5 (a)–(f) 2D-GIWAXS patterns and corresponding line-cut profiles of binary and ternary blend films. (g)–(l) TEM images of binary and ternary blend films.

17408 | *J. Mater. Chem. C*, 2024, **12**, 17403–17410

This journal is © The Royal Society of Chemistry 2024

20 wt%, 40 wt%, 60 wt%, 80 wt%, and 100 wt%, respectively, as shown in Fig. 4f. The ratios of $\mu_{\text{h}}/\mu_{\text{e}}$ are listed in Table S5 (ESI†). Faster and more balanced charge transfer in the ternary devices also contribute to the improvement of J_{SC} and PCE.

Ordered molecular stacking in the active layer plays an important role in the charge transfer. 2D GIWAXS patterns and line-cut profiles of binary and ternary blend films are shown in Fig. 5a–f, and the corresponding parameters are listed in Table S6 (ESI†). In addition, the 2D-GIWAXS patterns of PM6, **Y6** and **L8BO-2O** neat films are shown in Fig. S23 (ESI†). It can be seen that all the blend films exhibit a face-on/edge-on mixed orientation. After adding the third component, the **PM6:Y6:L8BO-2O** ternary blend films exhibit slightly enhanced out-of-plane (OOP) 010 peaks, indicating the enhanced π–π stacking of molecules. It is noteworthy that all binary and ternary films exhibit very similar stacking distances (3.60 Å). The similar geometry structures and intermolecular stacking distances of the two selected acceptors once again confirm their good miscibility, which is conducive to constructing more effective interaction modes between the third component and host system. Furthermore, the crystal coherence length (CCL)[47] calculated from the (010) peak of the OOP direction for the blend films is 29.09 Å (0 wt%), 31.75 Å (20 wt%), 31.23 Å (40 wt%), 30.39 Å (60 wt%), and 28.96 Å (100 wt%), respectively. The strengthened π–π stacking and increased CCLs are beneficial for charge transfer and extraction in ternary devices.

The transmission electron microscopy (TEM) images of the binary and ternary blend films are shown in Fig. 5g–l. Compared to the host **PM6:Y6** system, the PM6:**L8BO-2O** blend films exhibit larger phase separation. As discussed above, the good miscibility, similar structure and stacking distance between **Y6** and **L8BO-2O** allow **L8BO-2O** to blend well into the **PM6:Y6** mixture. As shown in the TEM images, the ternary blend films exhibit a similar morphology to the **PM6:Y6** host system even if the third component reaches 80 wt% in acceptors. This harmonious stacking distribution is very conducive to the synergistic effect of the two acceptors in the active layer to achieve more effective photoelectric conversion.

Conclusion

In this work, we designed and synthesized a novel non-fullerene acceptor **L8BO-2O** with an alkoxy chain as the third component, which can effectively suppress the aggregation effect of the active materials (**PM6:Y6**) and promote its appropriate phase separation during the film-formation process in high boiling point solvents. Meanwhile, the harmonious stacking constructed by the similar structure and stacking distance between **L8BO-2O** and **Y6** promotes more efficient energy transfer and alloy model working mechanism and significantly increases the mixing tolerance. As a result, with the doping of 20 wt% **L8BO-2O**, the efficiency of the champion ternary OSCs reached 16.4%. Also, within the wide doping range of **L8BO-2O** (0–80 wt%), the performance of all the ternary OSCs is significantly improved. The introduction of a high mixed tolerant third component,

which can inhibit molecular aggregation, not only effectively improves the performance of OSCs in high boiling point solvents but also significantly reduces the difficulty of device manufacturing and increases the repeatability of devices.

Data availability

The data that support the findings of this study are available in the ESI,† of this article or from the corresponding authors upon reasonable request.

Conflicts of interest

The authors declare no competing interests.

Acknowledgements

References

1 T. R. Andersen, H. F. Dam, M. Hösel, M. Helgesen, J. E. Carlé, T. T. Larsen-Olsen, S. A. Gevorgyan, J. W. Andreasen, J. Adams, N. Li, F. Machui, G. D. Spyropoulos, T. Ameri, N. Lemaître, M. Legros, A. Scheel, D. Gaiser, K. Kreul, S. Berny, O. R. Lozman, S. Nordman, M. Välimäki, M. Vilkman, R. R. Søndergaard, M. Jørgensen, C. J. Brabec and F. C. Krebs, *Energy Environ. Sci.*, 2014, **7**, 2925–2933.

2 W. Huang, Z. Jiang, K. Fukuda, X. Jiao, C. R. McNeill, T. Yokota and T. Someya, *Joule*, 2020, **4**, 128–141.

3 M. Kaltenbrunner, M. S. White, E. D. Głowacki, T. Sekitani, T. Someya, N. S. Sariciftci and S. Bauer, *Nat. Commun.*, 2012, **3**, 770.

4 F. C. Krebs, *Sol. Energy Mater. Sol. Cells*, 2009, **93**, 394–412.

5 H. Yu, J. Wang, Q. Zhou, J. Qin, Y. Wang, X. Lu and P. Cheng, *Chem. Soc. Rev.*, 2023, **52**, 4132–4148.

6 J. Wang, C. Han, S. Wen, F. Bi, Z. Hu, Y. Li, C. Yang, X. Bao and J. Chu, *Energy Environ. Sci.*, 2023, **16**, 2327–2337.

7 Y. Lin, J. Wang, Z. Zhang, H. Bai, Y. Li, D. Zhu and X. Zhan, *Adv. Mater.*, 2015, **27**, 1170–1174.

8 J. Yuan, T. Huang, P. Cheng, Y. Zou, H. Zhang, J. L. Yang, S. Chang, Z. Zhang, W. Huang, R. Wang, D. Meng, F. Gao and Y. Yang, *Nat. Commun.*, 2019, **10**, 570.

9 J. Fu, Q. Yang, P. Huang, S. Chung, K. Cho, Z. Kan, H. Liu, X. Lu, Y. Lang, H. Lai, F. He, P. W. K. Fong, S. Lu, Y. Yang, Z. Xiao and G. Li, *Nat. Commun.*, 2024, **15**, 1830.

This journal is © The Royal Society of Chemistry 2024

J. Mater. Chem. C, 2024, **12**, 17403–17410 | **17409**

10 Y. Sun, L. Wang, C. Guo, J. Xiao, C. Liu, C. Chen, W. Xia, Z. Gan, J. Cheng, J. Zhou, Z. Chen, J. Zhou, D. Liu, T. Wang and W. Li, *J. Am. Chem. Soc.*, 2024, **146**, 12011–12019.

11 C. Han, J. Wang, S. Zhang, L. Chen, F. Bi, J. Wang, C. Yang, P. Wang, Y. Li and X. Bao, *Adv. Mater.*, 2023, **35**, 2208986.

12 J. Wang, Q. Luan, P. Wang, C. Han, F. Bi, C. Yang, Y. Li and X. Bao, *Adv. Funct. Mater.*, 2023, **33**, 2301575.

13 D. Lee, C. Oh, J. Ryu, S. Jang, I. Hwang and S. Cho, *Mater. Adv.*, 2023, **4**, 4869–4876.

14 L. Zhu, M. Zhang, G. Zhou, T. Hao, J. Xu, J. Wang, C. Qiu, N. Prine, J. Ali, W. Feng, X. Gu, Z. Ma, Z. Tang, H. Zhu, L. Ying, Y. Zhang and F. Liu, *Adv. Energy Mater.*, 2020, **10**, 1904234.

15 X. Dong, Y. Jiang, L. Sun, F. Qin, X. Zhou, X. Lu, W. Wang and Y. Zhou, *Adv. Funct. Mater.*, 2022, **32**, 2110209.

16 Y. Cui, H. Yao, J. Zhang, K. Xian, T. Zhang, L. Hong, Y. Wang, Y. Xu, K. Ma, C. An, C. He, Z. Wei, F. Gao and J. Hou, *Adv. Mater.*, 2020, **32**, 1908205.

17 K. Jiang, Q. Wei, J. Y. L. Lai, Z. Peng, H. K. Kim, J. Yuan, L. Ye, H. Ade, Y. Zou and H. Yan, *Joule*, 2019, **3**, 3020–3033.

18 W. Zhao, S. Li, H. Yao, S. Zhang, Y. Zhang, B. Yang and J. Hou, *J. Am. Chem. Soc.*, 2017, **139**, 7148–7151.

19 P. Wang, F. Bi, Y. Li, C. Han, N. Zheng, S. Zhang, J. Wang, Y. Wu and X. Bao, *Adv. Funct. Mater.*, 2022, **32**, 2200166.

20 M. Liu, X. Ge, X. Jiang, F. Guo, S. Gao, Q. Peng, L. Zhao and Y. Zhang, *Adv. Funct. Mater.*, 2023, **33**, 2300214.

21 J. Lv, H. Tang, J. Huang, C. Yan, K. Liu, Q. Yang, D. Hu, R. Singh, J. Lee, S. Lu, G. Li and Z. Kan, *Energy Environ. Sci.*, 2021, **14**, 3044–3052.

22 Z. Zheng, E. He, J. Wang, Z. Qin, T. Niu, F. Guo, S. Gao, Z. Ma, L. Zhao, X. Lu, Q. Xue, Y. Cao, G. T. Mola and Y. Zhang, *J. Mater. Chem. A*, 2021, **9**, 26105–26112.

23 L. Zhong, Z. Sun, S. Lee, S. Jeong, S. Jung, Y. Cho, J. Park, J. Park, S. Yoon and C. Yang, *Adv. Funct. Mater.*, 2023, **33**, 2305450.

24 C. Yang, M. Jiang, S. Wang, B. Zhang, P. Mao, H. Y. Woo, F. Zhang, J. Wang and Q. An, *Adv. Mater.*, 2024, **36**, 2305356.

25 H. Chen, R. Zhang, X. Chen, G. Zeng, L. Kobera, S. Abbrent, B. Zhang, W. Chen, G. Xu, J. Oh, S.-H. Kang, S. Chen, C. Yang, J. Brus, J. Hou, F. Gao, Y. Li and Y. Li, *Nat. Energy*, 2021, **6**, 1045–1053.

26 J. Wang, C. Han, J. Han, F. Bi, X. Sun, S. Wen, C. Yang, C. Yang, X. Bao and J. Chu, *Adv. Energy Mater.*, 2022, **12**, 2201614.

27 M. Liu, X. Ge, X. Jiang, D. Chen, F. Guo, S. Gao, Q. Peng, L. Zhao and Y. Zhang, *Nano Energy*, 2023, **112**, 108501.

28 H. Chen, W. Sun, R. Zhang, Y. Huang, B. Zhang, G. Zeng, J. Ding, W. Chen, F. Gao, Y. Li and Y. Li, *Adv. Mater.*, 2024, **36**, 2402350.

29 Y. Huang, H. Chen, Q. Fan, Z. Chen, J. Ding, H. Yang, Z. Sun, R. Zhang, W. Chen, C. Yang, F. Gao and Y. Li, *Chin. J. Chem.*, 2023, **41**, 1066–1074.

30 Q. An, F. Zhang, J. Zhang, W. Tang, Z. Deng and B. Hu, *Energy Environ. Sci.*, 2016, **9**, 281–322.

31 N. Gasparini, X. Jiao, T. Heumueller, D. Baran, G. J. Matt, S. Fladischer, E. Spiecker, H. Ade, C. J. Brabec and T. Ameri, *Nat. Energy*, 2016, **1**, 16118.

32 Y. Li, Y. Cai, Y. Xie, J. Song, H. Wu, Z. Tang, J. Zhang, F. Huang and Y. Sun, *Energy Environ. Sci.*, 2021, **14**, 5009–5016.

33 J. Wang, C. Han, F. Bi, D. Huang, Y. Wu, Y. Li, S. Wen, L. Han, C. Yang, X. Bao and J. Chu, *Energy Environ. Sci.*, 2021, **14**, 5968–5978.

34 J. Wang, Y. Li, C. Han, L. Chen, F. Bi, Z. Hu, C. Yang, X. Bao and J. Chu, *Energy Environ. Sci.*, 2024, **17**, 4216–4227.

35 L. Zhan, S. Li, T. Lau, Y. Cui, X. Lu, M. Shi, C. Li, H. Li, J. Hou and H. Chen, *Energy Environ. Sci.*, 2020, **13**, 635–645.

36 C. Zhang, X. Zhong, X. Sun, J. Lv, Y. Ji, J. Fu, C. Zhao, Y. Yao, G. Zhang, W. Deng, K. Wang, G. Li and H. Hu, *Adv. Sci.*, 2024, **11**, 2401313.

37 S. Nilsson, A. Bernasik, A. Budkowski and E. Moons, *Macro-molecules*, 2007, **40**, 8291–8301.

38 J. Comyn, *Int. J. Adhes. Adhes.*, 1992, **12**, 145–149.

39 K.-H. Kim, H. Kang, H. J. Kim, P. S. Kim, S. C. Yoon and B. J. Kim, *Chem. Mater.*, 2012, **24**, 2373–2381.

40 Y. Cai, Y. Li, R. Wang, H. Wu, Z. Chen, J. Zhang, Z. Ma, X. Hao, Y. Zhao, C. Zhang, F. Huang and Y. Sun, *Adv. Mater.*, 2021, **33**, 2101733.

41 S. Karuthedath, J. Gorenflot, Y. Firdaus, N. Chaturvedi, C. S. P. De Castro, G. T. Harrison, J. I. Khan, A. Markina, A. H. Balawi, T. A. D. Peña, W. Liu, R. Liang, A. Sharma, S. H. K. Paleti, W. Zhang, Y. Lin, E. Alarousu, S. Lopatin, D. H. Anjum, P. M. Beaujuge, S. De Wolf, I. McCulloch, T. D. Anthopoulos, D. Baran, D. Andrienko and F. Laquai, *Nat. Mater.*, 2021, **20**, 378–384.

42 J.-S. Huang, T. Goh, X. Li, M. Y. Sfeir, E. A. Bielinski, S. Tomasulo, M. L. Lee, N. Hazari and A. D. Taylor, *Nat. Photonics*, 2013, **7**, 479–485.

43 S. Karuthedath, Y. Firdaus, R. Liang, J. Gorenflot, P. M. Beaujuge, T. D. Anthopoulos and F. Laquai, *Adv. Energy Mater.*, 2019, **9**, 1901443.

44 P. W. M. Blom, V. D. Mihailetchi, L. J. A. Koster and D. E. Markov, *Adv. Mater.*, 2007, **19**, 1551–1566.

45 A. K. K. Kyaw, D. H. Wang, V. Gupta, W. L. Leong, L. Ke, G. C. Bazan and A. J. Heeger, *ACS Nano*, 2013, **7**, 4569–4577.

46 L. J. A. Koster, V. D. Mihailetchi, R. Ramaker and P. W. M. Blom, *Appl. Phys. Lett.*, 2005, **86**, 123509.

47 D. M. Smilgies, *J. Appl. Crystallogr.*, 2009, **42**, 1030–1034.

17410 | *J. Mater. Chem. C*, 2024, **12**, 17403–17410

This journal is © The Royal Society of Chemistry 2024